



Experimental and 3-D Numerical Heat Transfer Analyses of Dual Spray Water Nozzle Impingement on a Flat Plate

Yu-Feng Gan¹ · Cheng-Chan Chien¹ · Jiin-Yuh Jang¹ · Chien-Nan Lin²

Received: 19 October 2019 / Accepted: 12 April 2020 / Published online: 20 April 2020
© Springer-Verlag GmbH Germany, part of Springer Nature 2020

Abstract

Spray impingement cooling is the major method currently used to cool steel after the hot-rolling process. In this study, dual nozzles are used to investigate the cooling character of the flat plate using for the spray impingement cooling process. Based on an experimental temperature measurement, a three-dimensional numerical model is set up to calculate the transient heat transfer coefficient of the cooling plate by solving the inverse heat conduction problem with the conjugate gradient method. Both the experimental and numerical results indicated that an interference region appeared between the two jet spray impingement regions. The interference pitch varied with the flow rates, the height from the plane to the jet outlet, and the distance between the two jets. As water spread over the plate, the heat dissipation region gradually stretched from the impingement region to the interference and flow regions. A peak in the heat flux curve was observed when the water arrived at the wet front of the flow. Meanwhile, the peak in the heat flux decreased as the distance from the impingement region increased. A maximum local heat transfer coefficient 23,000 W/(m²K) was observed in this experiment. The global average heat transfer coefficient increased with increases in the water flow rate, but it decreased with increases in the pitch.

Nomenclature

C_p	specific heat, J/(kgK)
H	the height of the nozzles relative to the flat plate, mm
h	heat transfer coefficient, W/(m ² K)
J_{obj}	objective function
k	thermal conductivity, W/(m ² K)
L	the length of the flat plate, mm
P	the pitch of the nozzles, mm
Q	the flow rate, L/min
q''	heat flux, MW/m ²
T	temperature, °C
t	the thickness of the flat plate, mm
W	the width of the flat plate, mm

Greek symbols

β	size of search step
γ	conjugate-gradient coefficient
ξ	search directions
ρ	density, kg/m ³

Subscripts

ave	average
es	estimate
ex	experiment
∞	environmental condition
m	search steps in the CGM
n	the number of variables
s	surface of the flat plate

1 Introduction

Spray impingement cooling is the main cooling process used after the hot-rolling process for steel to retain a fine crystal structure and to obtain better mechanical properties. The spray impingement cooling process utilizes the latent heat from evaporation to remove a large amount of heat from the plate when it leaves the hot rolling machine. A large temperature difference between the plate and the spray water results in a pool boiling heat transfer, which lead to a much higher heat transfer rate than can be achieved using a forced convection process. Many studies on the impingement cooling process have been conducted. For the study of a single nozzle, Chiu and Lin [1] investigated the dynamic behavior of a liquid-liquid compound drop impinging on a hot surface above the Leidenfrost temperature. The experimental results show that

✉ Jiin-Yuh Jang
jangjim@mail.ncku.edu.tw

¹ Department of Mechanical Engineering, National Cheng Kung University, Tainan 70101, Taiwan, People's Republic of China

² Department of Mechanical Engineering, Far East University, Tainan 74448, Taiwan, People's Republic of China

an increasing core-to-shell mass ratio raises the momentum loss, reduces the number of secondary drops, and promotes core-drop escaping. Leocadio et al. [2] conducted a study on the heat transfer behavior of a high-temperature steel plate cooled using a subcooled impingement circular water jet based on both experimental and numerical analyses. The results showed that the water jet can touch the hot strip surface without the formation of a vapor film. Karwa et al. [3] performed an experimental study of the heat transfer occurring during quenching of a cylindrical stainless steel test specimen and obtained the boiling curve and the heat transfer distributions for impingement velocities of 2.85 and 6.5 m/s. Gradeck et al. [4] studied the heat transfer from a hot moving cylinder impinged using a planar subcooled water jet and obtained the time-dependent surface temperature and extracted heat flux.

Wang et al. [5] investigated the heat transfer phenomena associated with a stationary hot steel plate during a water jet impingement cooling process. The local surface convection heat transfer coefficients and corresponding temperatures were calculated using a 2D finite difference program. The results revealed that the heat transfer coefficients were nonlinear functions of the surface temperature and that the cooling flow rate had no effect on the heat transfer coefficient and the surface temperature of the stagnation point. Dou et al. [6] deduced the surface heat flux by using an inverse heat conduction analysis based on an experimental study. Their results showed that heat transfer can be improved by increasing the surface roughness of the steel plate. Fu et al. [7] investigated ultra-fast cooling of a steel plate under spray cooling conditions. The results indicated that the spray inclination angle affects the cooling range of the plate by changing the spray injection zone area, flow density, and flow velocity, etc. Wang et al. [8] investigated the effect of the initial surface temperature, water temperature, and jet velocity on the heat transfer characteristics of a circular jet nozzle. It was found that the maximum heat flux was influenced by the initial surface temperature, water temperature, and jet velocity. Kahani et al. [9] presented the results of an experimental investigation of nanofluid droplets impacting on nanostructured surfaces. The results show that the increase in nanofluid concentration leads to a decrease in the maximum spreading and the height of droplets after impingement, and the use of nanofluids increases the temperature difference at the center of the droplet impact region.

For the study of multiple nozzles, Hall et al. [10] firstly successfully attempted to systematically predict the temperature response of a quenched part from knowledge of only the part geometry and spray nozzle configuration. Horacek et al. [11] studied time-varied and space-resolved heat transfer on a nominally isothermal surface cooled using two spray nozzles and an array of individually controlled microheaters. The results showed that the interaction between the two sprays was insignificant under their testing conditions and that the heat

flux of a single nozzle was comparable to that of two nozzles. In addition, the heat transfer increased significantly with decreases in the nozzle-to-heater spacing. Horsky et al. [12] presented an experimental method for measurement of heat transfer parameters for commonly used mist nozzles, where the pressure setting, casting speed, and behavior in the overlapping areas could all be tested. They also described the distribution of the heat transfer coefficient on the cooled steel surface.

Shtevi et al. [13] tested a number of differently constructed nozzles in order to verify whether these nozzles are appropriate to use in arrays for water spray quenching. The results showed that the optimal nozzle-to-nozzle distance was different from that predicted by ignoring the effect of droplet interaction, which resulted in uneven distribution of the mass flux density. Stark et al. [14] suggested that heat transfer rates vary with the applied flow parameters and their influence on the cooling conditions. Their results were examined with an experimental analysis of impinging multiphase jets and sprays. Horsky et al. [15] improved the efficiency of the nozzle cooling system by changing the type of nozzle, geometrical configuration (nozzles pitch, distance from the roll, orientation, number of manifolds), coolant pressure, and temperature in a roll cooling process. Pohanka and Votavova [16] studied multiple spray water nozzle impingement on a steel surface to remove unwanted scales during the production process. Interference zones were formed between the nozzles, because the nozzles were arranged in-line. The heat transfer coefficient and surface temperature of the interference zone was compared with the undisturbed areas, and the results showed the interference zone to be grossly overcooled.

These previous studies indicated that many parameters affect the heat transfer coefficients of a flat plate under spray cooling conditions. In addition, the heat transfer coefficient significantly changes the heat dissipation rate of the hot plate, thus affecting the temperature distribution. In order to obtain the heat transfer coefficient profile of a flat plate during the impingement cooling process, an inverse calculation method is typically adopted to solve the profile, using the temperature obtained from the commercial CFD code ANSYS FLUENT. The solver combined with the conjugate-gradient method (CGM) that has been successfully applied to other applications [17–21].

The nozzle arrays are widely used in the plate cooling, both the pitch of nozzles and the water flow rate are important parameters that significantly affect the heat transfer coefficient distribution for a flat plate during the spray impingement cooling process. However, there has been little study or analysis of the transient heat transfer coefficient distribution on the interference effect of dual spray impingement nozzles with different pitches and water flow rates. This gap in the literature has motivated the present investigation, and this study aims to

discuss the influence of nozzle pitch and nozzle flow rate for the heat transfer rate.

2 Mathematical analysis

In this work, the controlled cooling process for a flat plate from the China Steel Corporation (CSC), Taiwan is discussed. A three-dimensional numerical model is used to simulate the transient heat transfer cooling process after the rolling process. The physical model and computational grid system of the flat plate are shown in Fig. 1(a) and (b). The flat plate used in this study was stainless steel with

dimensions of 300 mm × 300 mm × 40 mm. Based on the cooling and the geometrical characteristics of the flat plate, a 1/4 symmetry physical model was adopted in the computational domain. The symmetry lines are along the x -axis and z -axis individually, so the 1/4 symmetry physical model was divided into 18 parts corresponding to the heat transfer coefficients h_1, h_2, h_3, \dots etc., and h_{18} based on the thermocouple positions and the flow track with different nozzle pitch, as shown in Fig. 1(c), which was divided into 6 segments along the x -direction uniformly and divided into 3 segments along the z -direction. In this research, the heat transfer coefficients were determined by solving the inverse heat conduction problem with a conjugate

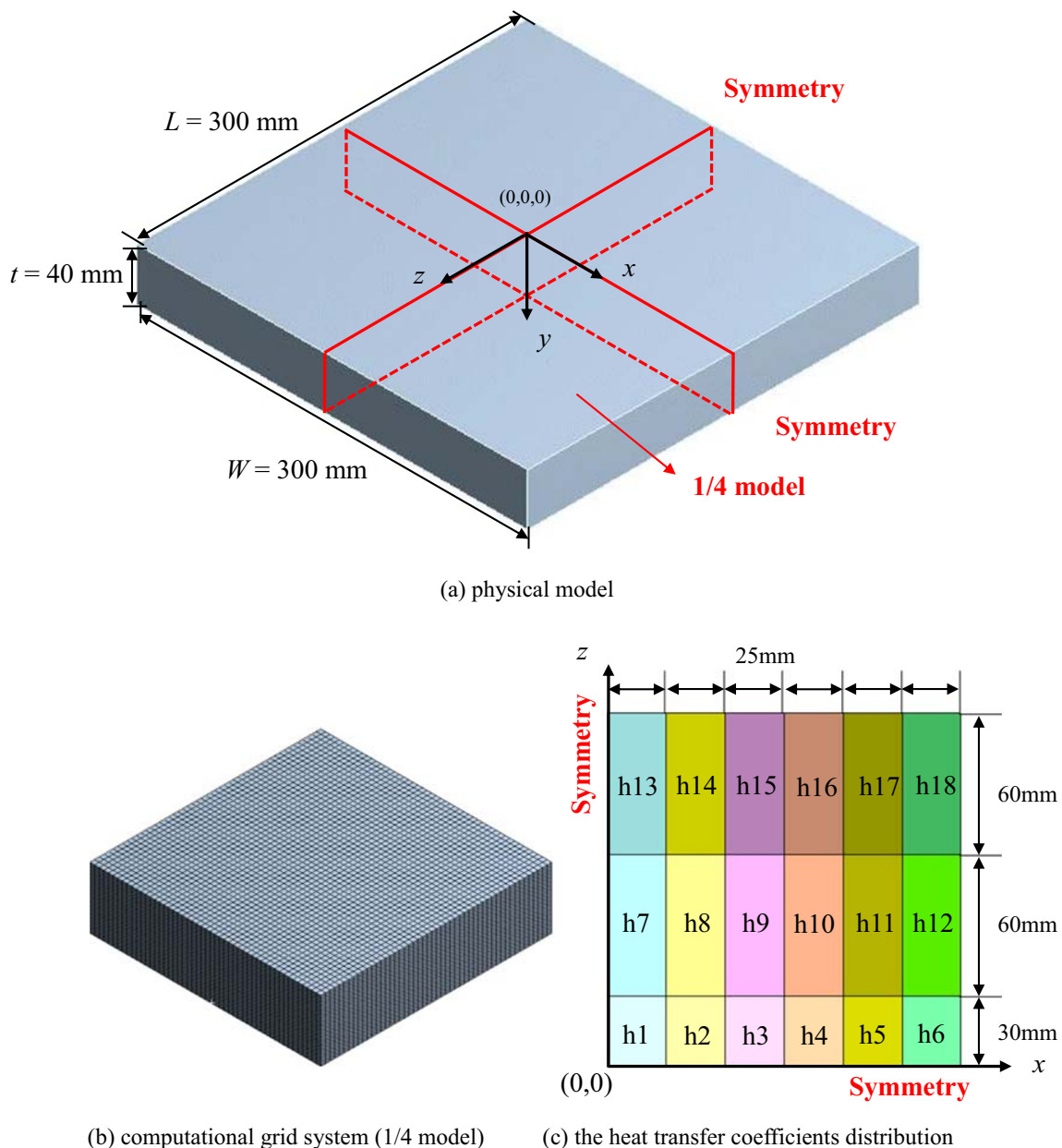


Fig. 1 Physical model, computational grid system, and the heat transfer coefficient distribution

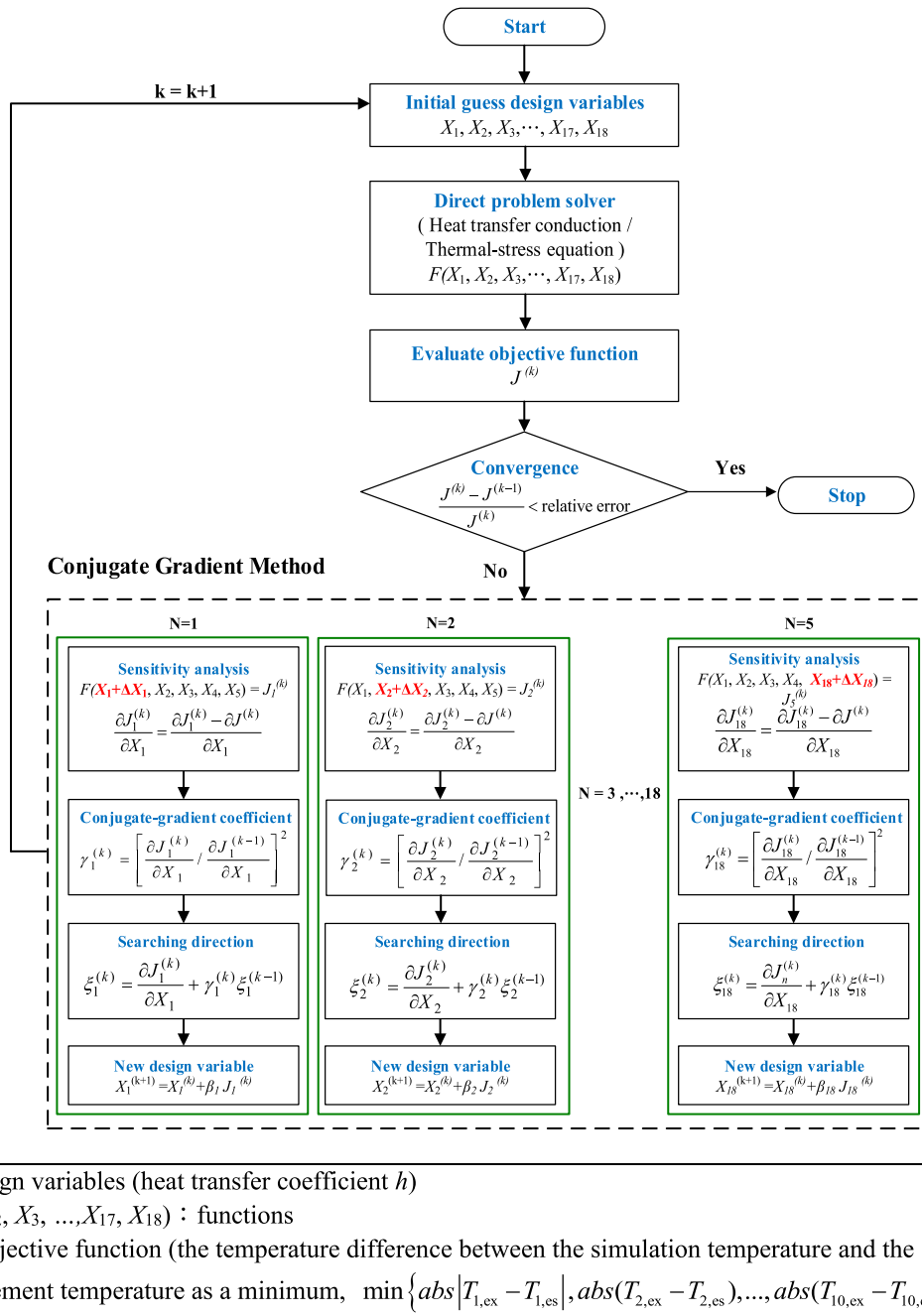


Fig. 2 A flowchart of the inverse calculation process

gradient method (CGM) search based on the local temperature distribution in the experiment.

2.1 Governing equations

The following transient conduction equation governs the temperature field of a flat plate

$$\frac{\partial}{\partial x_j} k \left(\frac{\partial T}{\partial x_j} \right) = \rho \cdot C_p \frac{\partial T}{\partial t}, \tag{1}$$

where ρ , C_p , and k are the density, heat capacity, and thermal conductivity of the flat plate, respectively. The density ρ is a constant equal to 7750 kg/m³, and correlation of the heat capacity and the thermal conductivity are varied with the temperature as follows [22].

$$C_p = 337.6747 + 0.8735T - 0.001469T^2 + 1 \times 10^{-6}T^3, \quad T \leq 700 \text{ K}, \tag{2}$$

$$k = 17.9148 - 0.0249T + 7.5396 \times 10^{-5}T^2 - 5.0021 \times 10^{-8}T^3, \quad T \leq 700 \text{ K}. \tag{3}$$

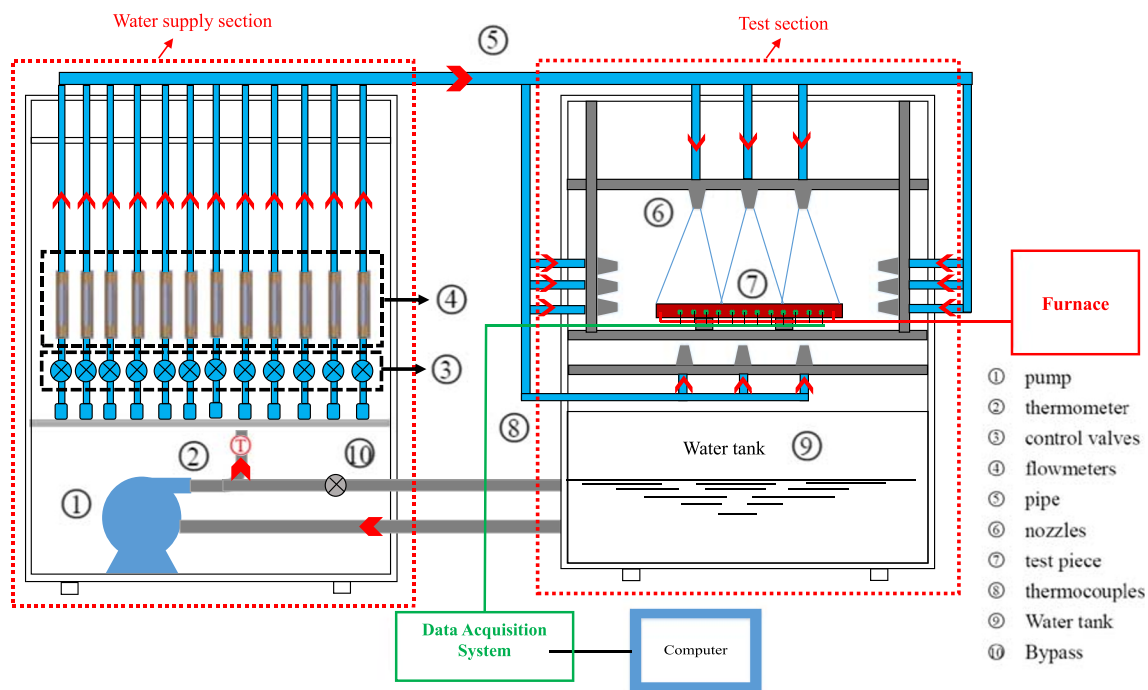


Fig. 3 Schematic of the experimental setup

2.2 Initial and boundary conditions

The initial temperature of the plate is at 400 °C. For the boundary conditions, the convective heat transfer between the flat plate surface and the surroundings is evaluated by using the following equation

$$q'' = -k \frac{\partial T}{\partial n} \Big|_{\text{sur face}} = h(T_s - T_\infty), \quad (4)$$

where h is the convective heat transfer coefficient for the surface of the flat plate and varies with the different parts of the flat plate, the convective heat transfer coefficient for the side and bottom of the plate are varied from 50 through 200 W/(m²K) in order to examine the sensibility of the inverse heat conduction calculation; T_s is the surface temperature of the flat plate, and T_∞ is the environmental temperature of 22 °C in the cooling process.

The averaged of heat transfer coefficient is defined as follows

$$h(t) = \frac{\iint h(x, z, t) dx dz}{L_x L_z}. \quad (5)$$

3 Numerical method

3.1 Numerical algorithm

In this study, Fluent commercial software was adopted to solve the governing equations, and the finite volume numerical

method was used to simulate the temperature field analysis. The computation process was transient, so the first order implicit method was adopted to maintain the numerical stability of every time step. The time step was 0.1 s for the CGM, which is sufficient to describe the globe temperature change for the cooling plate and the computational accuracy requirements. A structured grid system is typically adopted in the computational domain. However, a careful check of the grid independence of the numerical solutions was made to ensure the accuracy and validity of the numerical results. For this purpose, three grid systems (59,536; 83,349; and 115,351) were tested. It was found that the relative errors in the local temperature between the solutions obtained with 83,349 and 115,351 grids were less than 0.5%. The discretized system was solved iteratively until it satisfied the following residual convergence criterion

$$\max \left(\frac{|T_{i,j}^n - T_{i,j}^{n-1}|}{T_{i,j}^n} \right) \leq 10^{-6}. \quad (6)$$

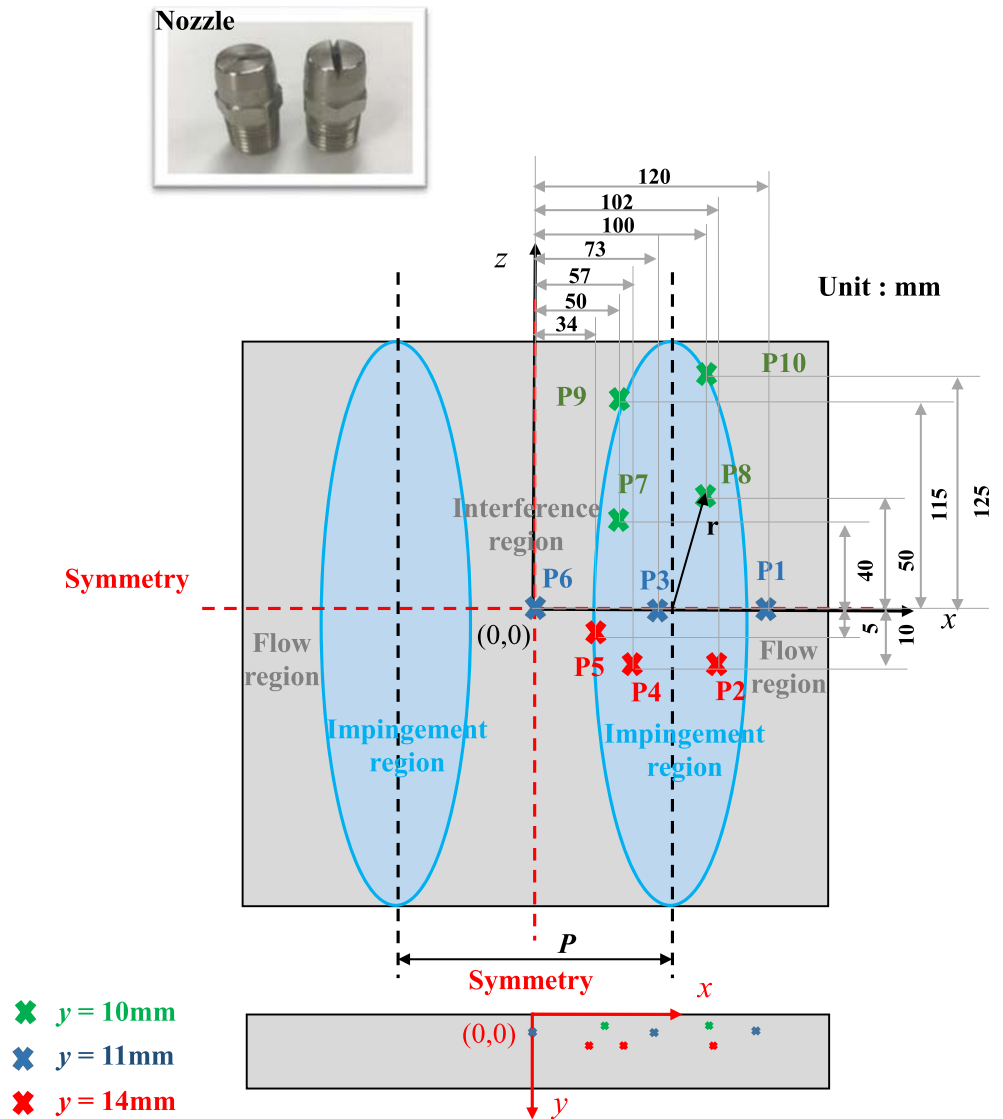
where $T_{i,j}^{n-1}$ is the previous temperature value of $T_{i,j}^n$ at the same time level.

The simulations were performed as a parallel calculation for the three-dimensional models on a sixteen core CPUs with 128G RAM working station computer. The computer computation times were approximately 20 min for each search step.

3.2 Inverse heat conduction method

In this study, based on the local temperature distribution used in the experiment, the conjugate-gradient method (CGM) was

Fig. 4 Thermocouple positions



combined with a finite volume method (FVM) code as a tool to search for the heat transfer coefficients. The objective function $J_{obj}(h_1, h_2, h_3, \dots, h_{17}, h_{18})$ was defined as the temperature difference between the simulation temperature and the measurement temperature as a minimum ($\min\{abs|T_{1, ex} - T_{1, es}|, abs|T_{2, ex} - T_{2, es}|, \dots, abs|T_{10, ex} - T_{10, es}|\}$).

Above all, the CGM method evaluates the gradient of the objective function, and then it sets up a new conjugate direction for the updated design variables with the help of a direct numerical sensitivity y analysis. The initial guess for the value of each search variable was made, and in the successive steps, the conjugate-gradient coefficients and the search directions were evaluated to estimate the new search variables. The solutions obtained from the finite volume method were then used to calculate the value of the objective function, which was further transmitted back to the optimizer for the purpose of calculating the consecutive directions. The procedure for applying this method is described as follows:

- (1) Generate an initial guess for eighteen design variables $(x_1, x_2, x_3, \dots, x_{17}, x_{18})$ – the heat transfer coefficients $(h_1, h_2, h_3, \dots, h_{17}, h_{18})$.
- (2) Adopt the finite difference method to predict the temperature fields $(T(x, z))$ associated with the last $(h_1, h_2, h_3, \dots, h_{17}, h_{18})$, and then calculate the objective function $J_{obj}(h_1, h_2, h_3, \dots, h_{17}, h_{18})$.
- (3) When the value of $J_{obj}(h_1, h_2, h_3, \dots, h_{17}, h_{18})$ reaches the minimum, the inverse search process is terminated. Otherwise, proceed to step (4).
- (4) Determine the gradient functions, $(\partial J_{obj} / \partial x_i)^{(m)}$ ($i = 1, 2, 3, \dots, 17, 18$), by applying a small perturbation $(\Delta x_1, \Delta x_2, \Delta x_3, \dots, \Delta x_{17}, \Delta x_{18})$ to each value of $(x_1, x_2, x_3, \dots, x_{17}, x_{18})$, and calculate the corresponding change in objective function $J_{obj}(h_1, h_2, h_3, \dots, h_{17}, h_{18})$. Then, the gradient functions with respect to each value of the design variables $(x_1, x_2, x_3, \dots, x_{17}, x_{18})$ can be calculated by the direct numerical differentiation as

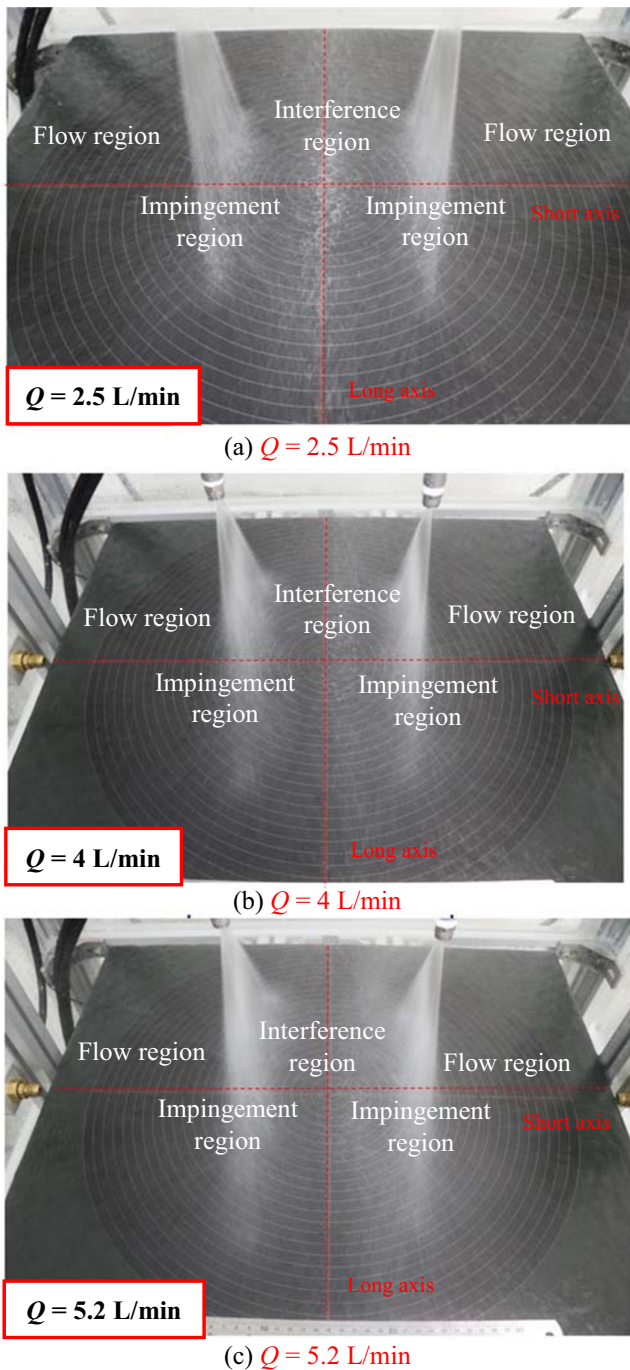


Fig. 5 Observation of the flow track under different flow rates ($H = 200$ mm, $P = 150$ mm)

$$\frac{\partial J_{obj}}{\partial x_1} = \frac{\Delta J_{obj}}{\Delta x_1}, \frac{\partial J_{obj}}{\partial x_2} = \frac{\Delta J_{obj}}{\Delta x_2}, \dots, \frac{\partial J_{obj}}{\partial x_{17}} = \frac{\Delta J_{obj}}{\Delta x_{17}}, \frac{\partial J_{obj}}{\partial x_{18}} = \frac{\Delta J_{obj}}{\Delta x_{18}} \quad (7)$$

(5) Calculate the conjugate-gradient coefficients, $\gamma^{(m)}$, and the search directions, $\xi_1^{(m+1)}, \xi_2^{(m+1)}, \xi_3^{(m+1)}, \dots, \xi_{17}^{(m+1)}$,

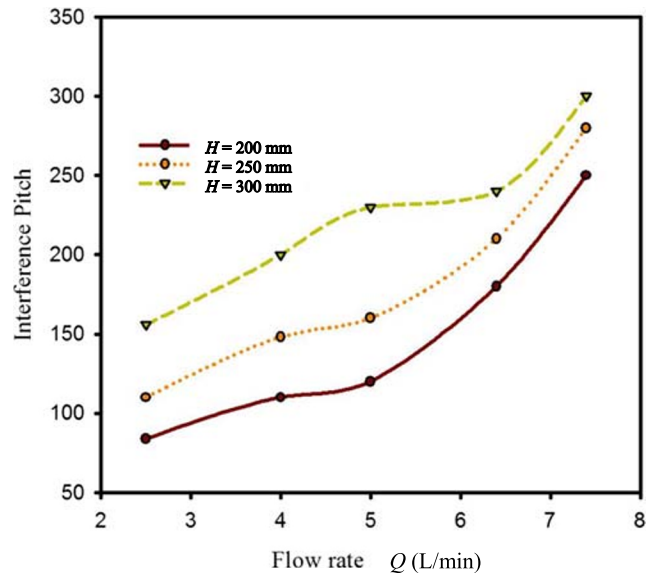


Fig. 6 The relationship of the interference pitch with different heights and flow rates

$\xi_{18}^{(m+1)}$, for the search variables. For the first step with $k = 1, \gamma^{(1)} = 0$.

$$\gamma^{(m)} = \left[\frac{2 \frac{\partial J_{obj}^{(m)}}{\partial x_n}}{\sum_n \frac{\partial J_{obj}^{(m)}}{\partial x_n}} / \frac{2 \frac{\partial J_{obj}^{(m-1)}}{\partial x_n}}{\sum_n \frac{\partial J_{obj}^{(m-1)}}{\partial x_n}} \right]^2, n = 1, 2, 3, \dots, 17, 18 \quad (8)$$

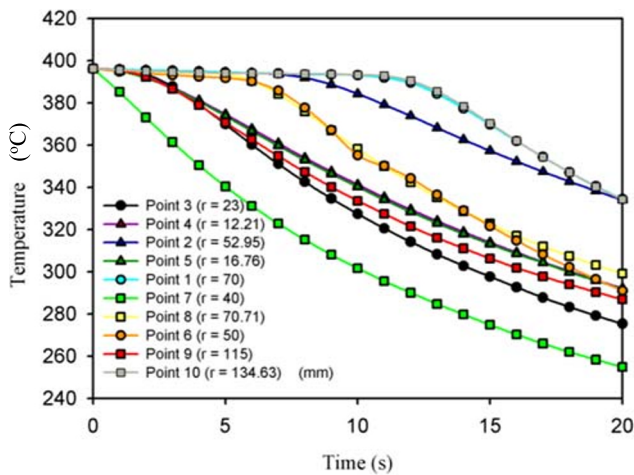
$$\begin{aligned} \xi_1^{(m+1)} &= \frac{\partial J_{obj}^{(m)}}{\partial x_1} + \gamma^{(m)} \xi_1^{(m)}, \xi_2^{(m+1)} \\ &= \frac{\partial J_{obj}^{(m)}}{\partial x_2} + \gamma^{(m)} \xi_2^{(m)}, \dots, \xi_{18}^{(m+1)} \\ &= \frac{\partial J_{obj}^{(m)}}{\partial x_{18}} + \gamma^{(m)} \xi_{18}^{(m)} \end{aligned} \quad (9)$$

(6) Assign values to the coefficients in a descending direction ($\beta_1, \beta_2, \beta_3, \dots, \beta_{17}, \beta_{18}$) for all values of the design variables ($x_1, x_2, x_3, \dots, x_{17}, x_{18}$). Specifically, these values are chosen using a trial and error process. In general, the coefficients in the descending direction ($\beta_1, \beta_2, \beta_3, \dots, \beta_{17}, \beta_{18}$) range from 1 to 50 based on trial and error.

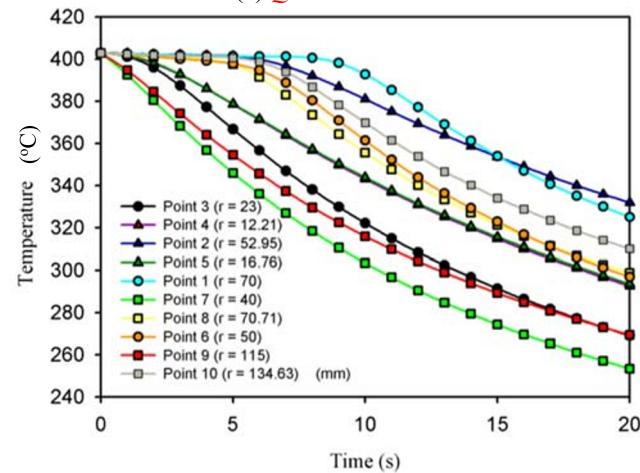
(7) Update the design variables with

$$\begin{aligned} x_1^{(m+1)} &= x_1^{(m)} + \beta_1 \xi_1^{(m)}, x_2^{(m+1)} \\ &= x_2^{(m)} + \beta_2 \xi_2^{(m)}, \dots, x_{18}^{(m+1)} = x_{18}^{(m)} + \beta_{18} \xi_{18}^{(m)} \end{aligned} \quad (10)$$

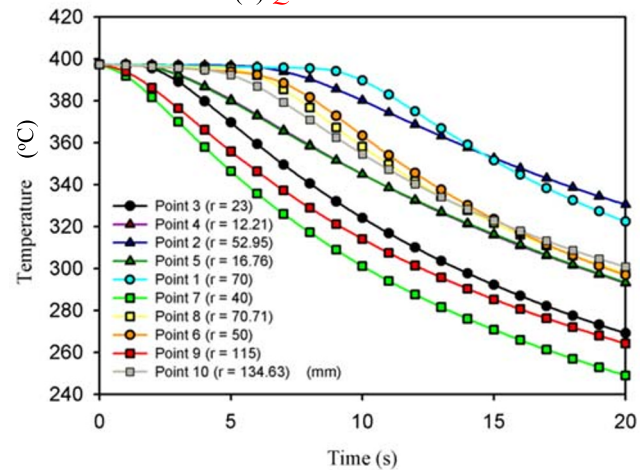
A flowchart of the inverse calculation process by using CGM is plotted as Fig. 2.



(a) $Q = 2.5$ L/min



(b) $Q = 4.0$ L/min



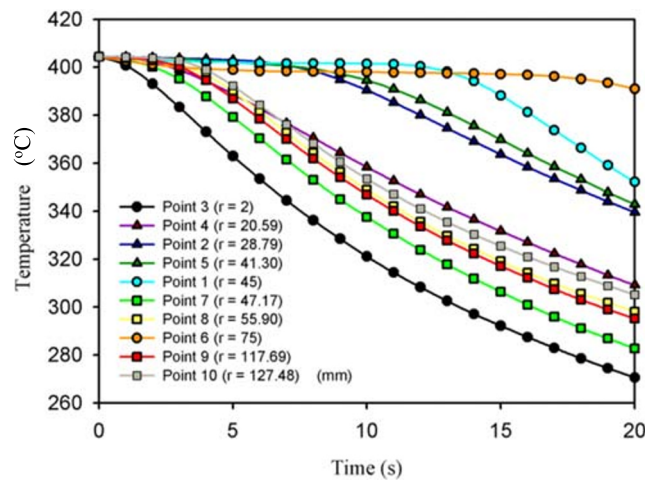
(c) $Q = 5.2$ L/min

Fig. 7 Measured cooling curves with different flow rate ($P = 100$ mm)

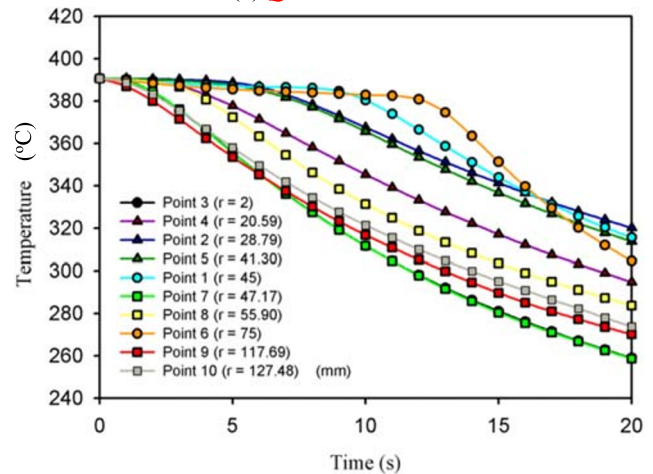
4 Experimental facilities and method

4.1 Experimental equipment and procedure

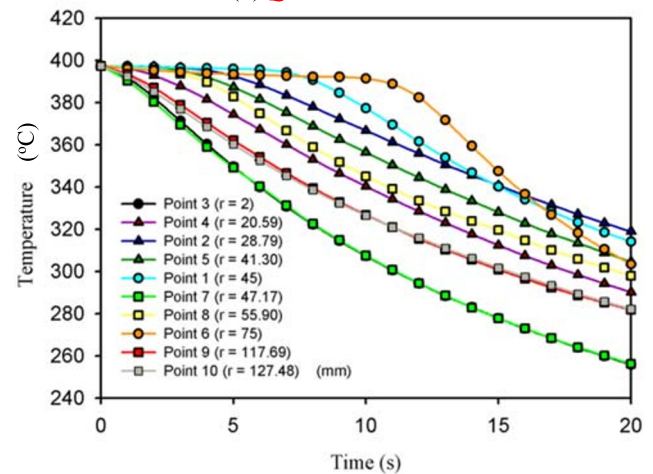
The experimental setup is illustrated schematically in Fig. 3. It consists of four parts: (1) the furnace, (2) the test section, (3)



(a) $Q = 2.5$ L/min



(b) $Q = 4.0$ L/min



(c) $Q = 5.2$ L/min

Fig. 8 Measured cooling curves with different flow rate ($P = 150$ mm)

the water supply system, and (4) data acquisition system. The furnace is used to heat the test piece to the desired temperature. The test section comprises the test piece, thermocouples, nozzles, and a water tank. The test piece is a flat plate, which is composed of the impingement region, the interference region

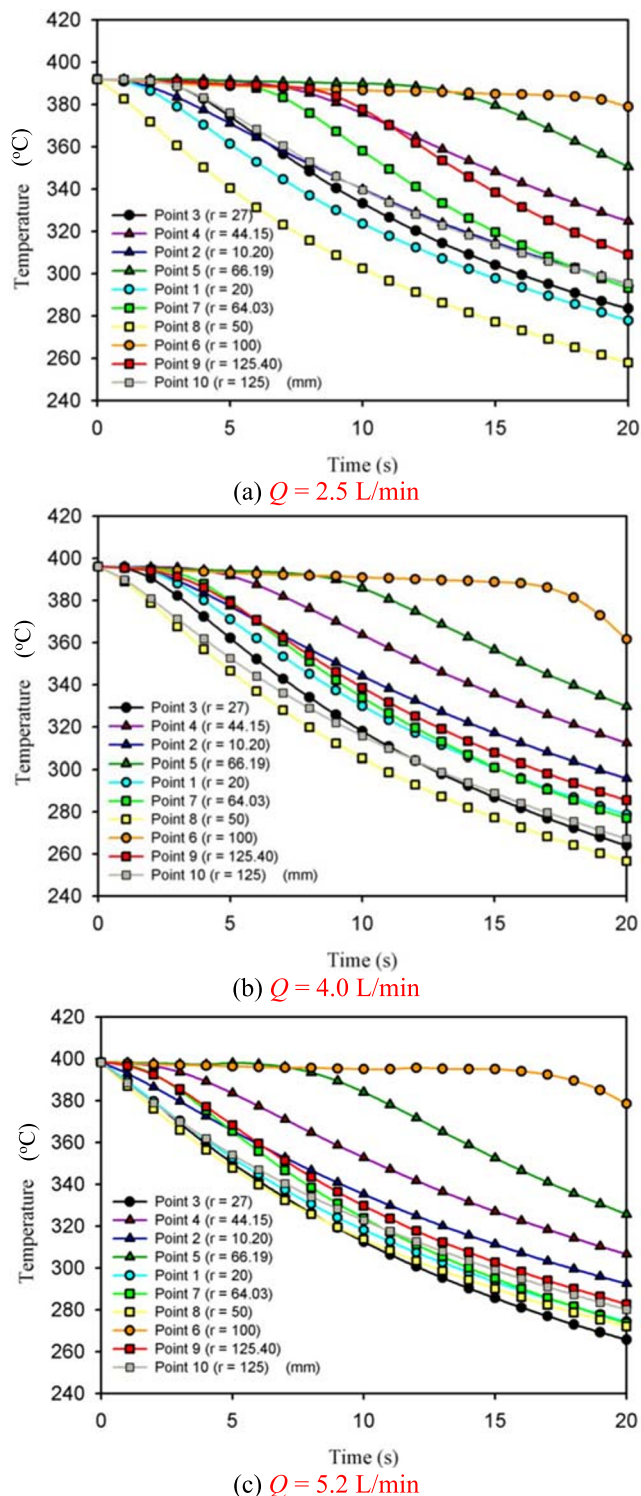


Fig. 9 Measured cooling curves with different flow rate ($P = 200$ mm)

and the flow region, as shown in Fig. 4. Total 10 thermocouples (type-K) are inserted into the hot plate at 10, 11 or 14 mm distance below the cooling surface to measure the time variation of the plate temperatures.

The water supply system includes a pump, thermometers, control valves, and flowmeters. The water flow rate of the

multiple spray water nozzles was controlled by the control valves and monitored by the flowmeters. Two VVP8080 nozzles (manufactured by Ikeuchi Taiwan Co., Ltd.) were used in all experiments, for which the angle is 80° , and the maximum of the water flow rate is 8 L/min under a pressure of 0.3 MPa with droplet size $290 \sim 550 \mu\text{m}$. The impingement region is in the shape of an ellipse, as shown in Fig. 4.

The experimental procedure was done as follows: (1) The test piece was first heated uniformly in the furnace 400°C ($\pm 5^\circ\text{C}$) and then was moved to the test section for spray cooling. (2) The nozzles were adjusted to a specific pitch and height. (3) The water flow rate was controlled by the control valves and monitored by the flowmeters to maintain a stable flow. Three different water flow rates (2.5 L/min, 4.0 L/min, and 5.2 L/min) were conducted in this study. (4) The local temperature of the flat plate and the water was monitored and recorded using the data acquisition system. (5) The flat plate was placed in the test table and impinged by the spray water nozzles for 20 s.

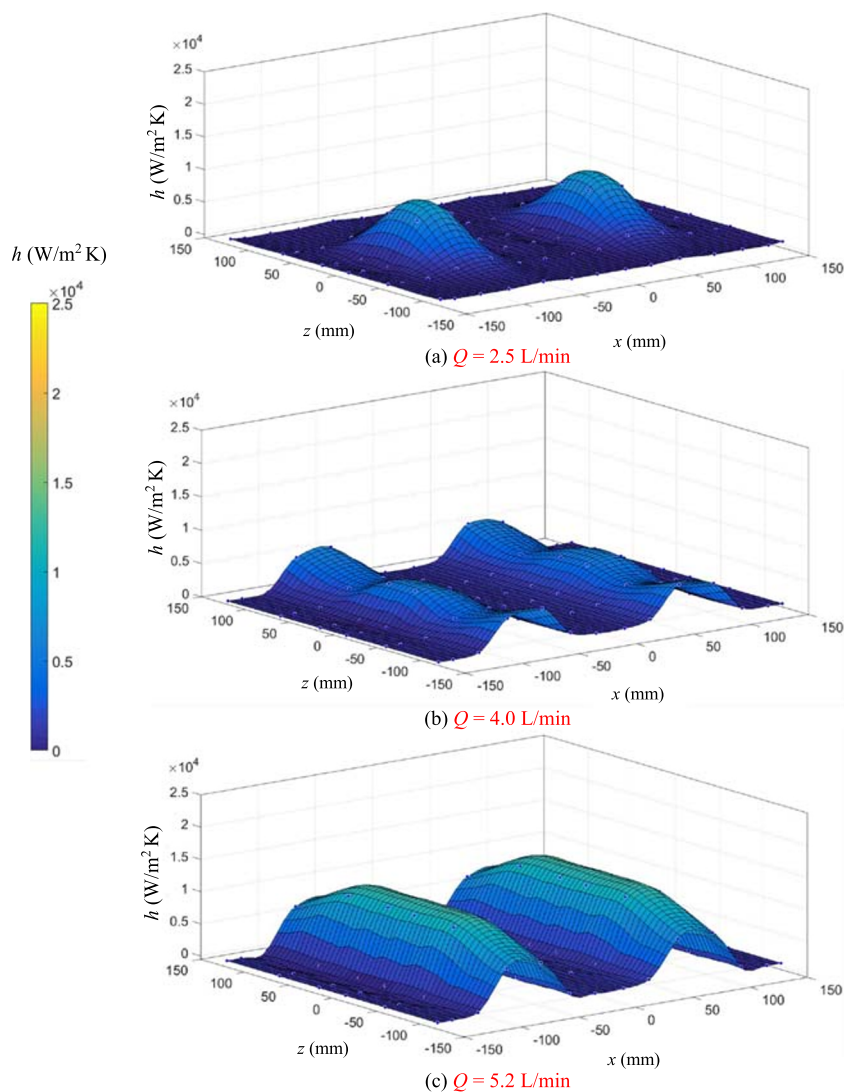
4.2 Experimental error analysis

Measurement errors can be divided into two components: random error and systematic errors. The thermocouples (type K) had an error of approximately $\pm 1^\circ\text{C}$. The accuracy of the data acquisition system for temperature (GRAPHTEC-GL840) was about $\pm 0.1^\circ\text{C}$. The water temperature of the nozzles was controlled within $\pm 0.5^\circ\text{C}$. The relative errors for the water flow rate and the thermocouples arrangement were approximately $\pm 2\%$ and $\pm 1\%$, respectively. The deviation is about $\pm 1\%$ for the boundary condition of the plate (the heat transfer coefficient of the side and bottom). In addition, to minimize the measurement precision uncertainty, three identical measurements were taken under the same circumstances, and then the average was taken. Using the method proposed by Kline and McClintock [23], the total uncertainty in the spray cooling curves obtained by combining the uncertainty in repeatability with the measurement inaccuracies was estimated to be 3.5%.

5 Results and discussion

In this study, the transient heat transfer analysis for dual spray water nozzle impingement on a flat plate was studied to obtain the local temperature distribution of the flat plate by considering the different water flow rates ($Q = 2.5, 4,$ and 5.2 L/min), and different nozzle pitches ($P = 100, 150,$ and 200 mm), which used to examine the influence of the nozzle parameters for the heat transfer rate. Based on the local temperature distribution of the flat plate, the inverse heat conduction problem with a three-dimensional numerical model was utilized to

Fig. 10 The heat transfer coefficient distribution with flow rate of $t = 1$ s ($P = 150$ mm)



obtain the heat transfer coefficients using a conjugate gradient method (CGM) search.

Figure 5 shows that the flow track under the different water flow rates ($Q = 2.5, 4,$ and 5.2 L/min) with a height of 200 mm and a pitch of 150 mm between the two nozzles. A black acrylic plate with marked scale was installed on the impingement surface to display the flow of the injected water. It is obvious that the flow track was divided into three parts: the impingement region, the interference region, and the flow region. The impingement region appeared as an ellipse and was located below the nozzles. It can be observed that the range of the impingement region increased with increases in the water flow rate. The interference region was located in the center of the impingement regions along the short-axis, and the interference effect was obviously enhanced with increases in the water flow rate. The flow region was located around the interference and impingement regions. Note that, while the cooling water jet initially hit the hot plate (about 400 °C),

the impingement region rapidly spread outward, and this phenomenon did not occur when the water jet hit the acrylic plate at room temperature without heating. This phenomenon has been verified by some researchers [2, 5, 8].

Figure 6 indicates the relationship of the interference pitch of nozzles at different heights and with different water flow rates, as obtained by observing the flow field. Based on the observation of the flow field, it was found that as the water flow rate and the height increased, the interference pitch also increased due to enhancement of the range of the impingement region. In order to investigate the influence of the interference effect on the heat transfer coefficient, different nozzle pitches and water flow rates were used as parameters for the experiment in this study. The height between the jet outlet and the impingement surface was set at 200 mm for all the cases referenced below.

Figures 7, 8, and 9 show the cooling curves at various locations of the hot plate with different water flow rates

($Q = 2.5, 4, \text{ and } 5.2 \text{ L/min}$) and different pitches ($P = 100, 150, \text{ and } 200 \text{ mm}$), respectively. Because the range of the impingement region, interference region, and flow region varied with the pitch and the water flow rate of the nozzle, the cooling curves for specific points exhibited different trends with the different water flow rates and different pitches. From the Figs, it can be seen that before the nozzles were turned on, the temperature of the hot plate was uniform for all experiments. When the water impinged the hot plate, the temperature of the impingement region dropped immediately and significantly and then decreased relatively slowly, as shown in the cooling curves at points 7, 3, and 8, individually. Figures 7, 8, and 9 denote nozzle pitches of 100, 150, and 200 mm, respectively. At the interference region (point 6) and the flow region (point 1), the temperature initially changed moderately, and then a sharp drop occurred from the center to the edge sequentially. At a pitch of 100 mm, the temperature at point 6 (located at the interference region) exhibited a sharp

drop at 7 s, which means the interference effect was generated at this moment. The temperature of point 1 exhibited a sharp drop at 10–12 s for the different flow rates, which means the vapor film gradually disappeared with the high-velocity flow. For the pitches of 150 mm and 200 mm (shown as Figs. 8 and 9), the cooling curves at various regions had the same trend.

Figures 10, 11, 12, 13, and 14 show the heat transfer coefficient distribution with different water flow rates ($Q = 2.5, 4, \text{ and } 5.2 \text{ L/min}$) at different times ($t = 1 \text{ s}, 5 \text{ s}, 10 \text{ s}, 15 \text{ s}, \text{ and } 20 \text{ s}$) at a pitch of 150 mm. The heat transfer coefficient can be seen as a nonlinear function of time and locations. At time $t = 1 \text{ s}$, an obvious difference in the heat transfer coefficient distribution can be seen with different water flow rates, as shown in Fig. 10, where the high heat transfer region is concentrated in the impingement region. Over time, the high heat transfer region gradually spread to the interference region and the flow region owing to the water flow, which resulted in the interference effect. In addition, it is obvious that the

Fig. 11 The heat transfer coefficient distribution with flow rate of $t = 5 \text{ s}$ ($P = 150 \text{ mm}$)

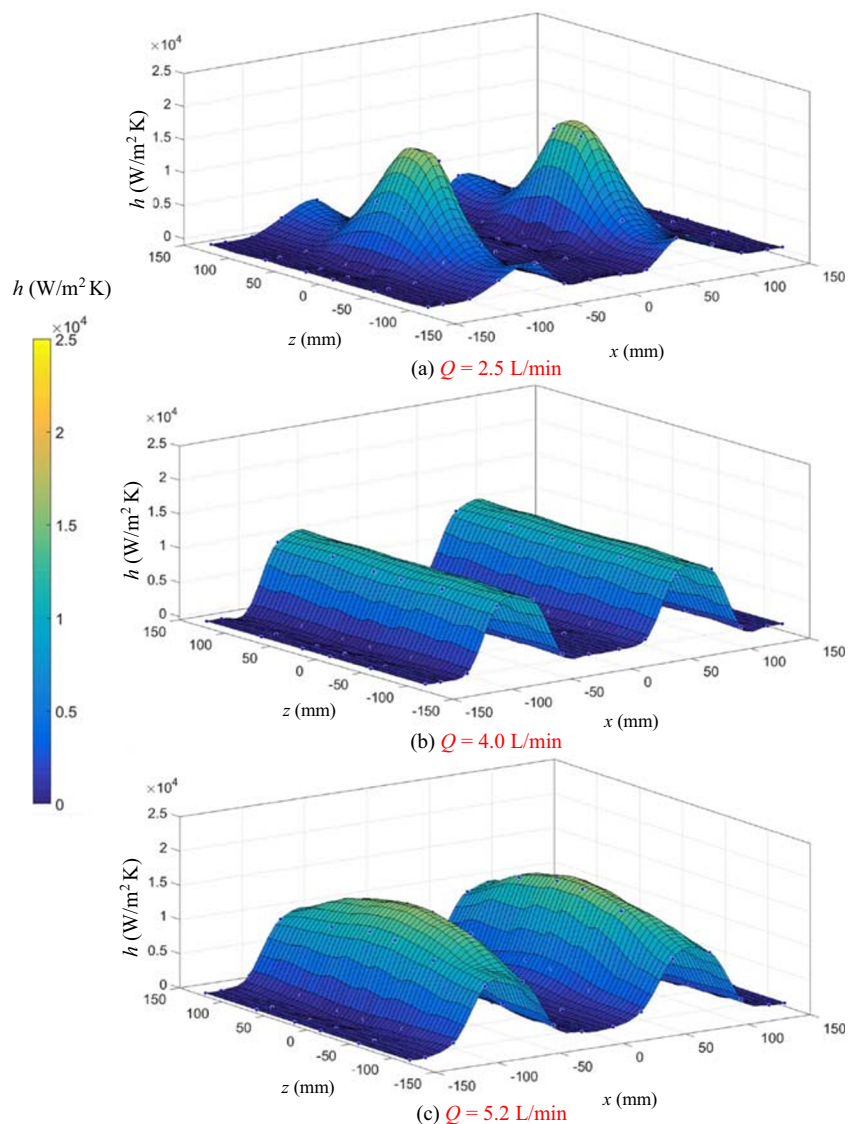
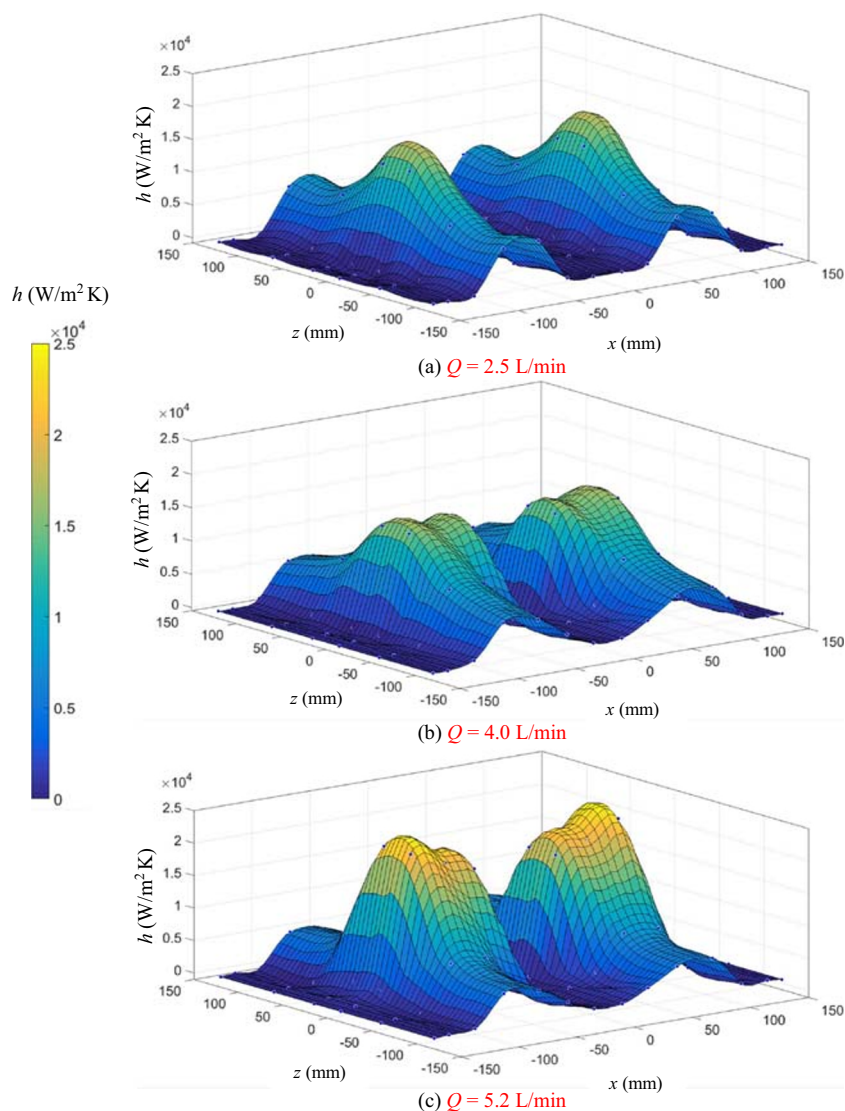


Fig. 12 The heat transfer coefficient distribution with flow rate of $t = 10$ s ($P = 150$ mm)

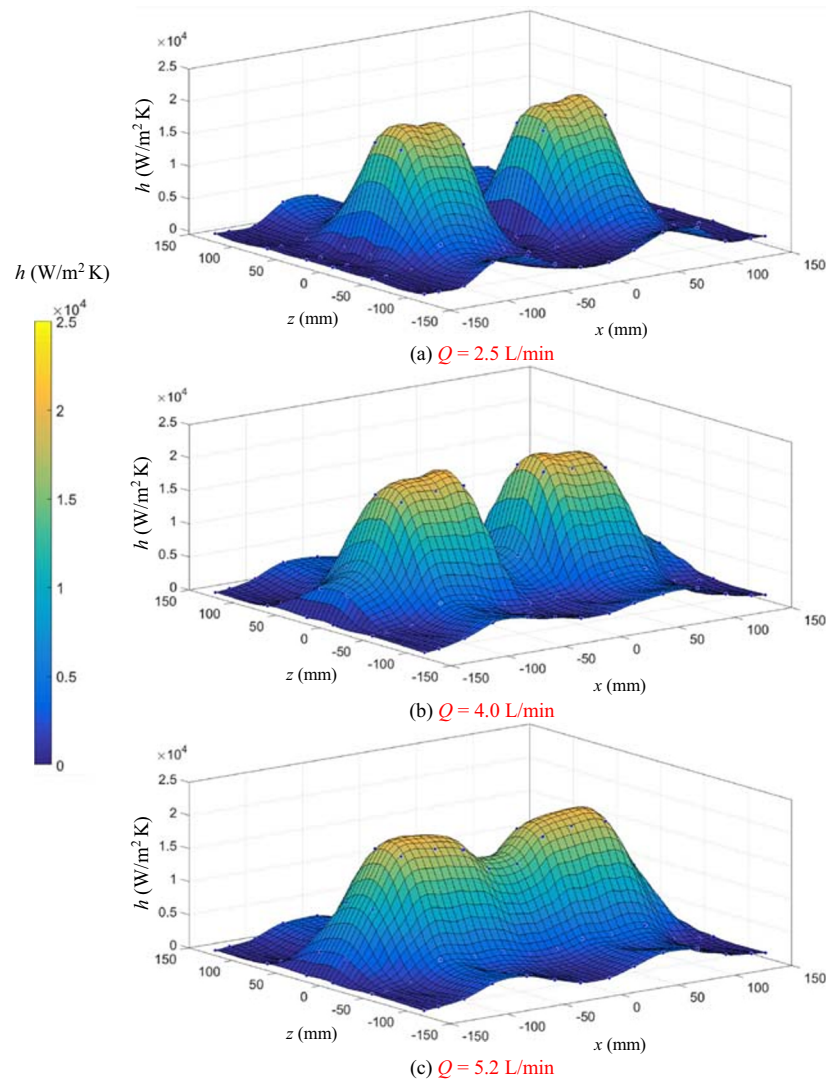


interference effect increased over time, as shown in Figs. 12 to 14, where the maximum heat transfer coefficient in the interference region was about $14,000 \text{ W}/(\text{m}^2\text{K})$ during the cooling process. Meanwhile, the heat transfer coefficient was larger than other regions, and a maximum heat transfer coefficient of $23,000 \text{ W}/(\text{m}^2\text{K})$ was achieved for the impingement region. As expected, the heat transfer coefficient in the flow region was the smallest.

Figure 15 shows the cooling curve and the corresponding time-varying heat transfer coefficient during the cooling process with a pitch of 150 mm and a water flow rate of 5.2 L/min for the three different regions, respectively. It was found that the temperature cooling curve and the heat transfer coefficient distribution were highly nonlinear with the time. In order to analyze the characteristic of the cooling curve and the heat transfer coefficient in the different regions, points 8, 1, and 6 were used to be representative of the impingement region, the flow region, and the interference region, respectively.

Figure 15(a) shows that the temperature of the impingement region (point 8) decreased slowly within 4 s and then decreased rapidly. The corresponding heat transfer coefficient increased slightly and then decreased during the cooling process. Figure 15(b) shows that the temperature of the flow region (point 1) decreased very slowly within 6 s due to the vapor film on the surface of the hot plate, and then the temperature decreased rapidly during a cooling time of 20 s because of the high-velocity flow of the water over the hot plate, thus eliminating the vapor film. The corresponding heat transfer coefficient curve remained at a lower value until the vapor film was eliminated. It then increased sharply from 6 s through 13 s, after which it decreased until 20 s. In addition, Fig. 15(c) shows the characteristics of the interference region (point 6) as the impingement region rapidly spread outward after the cooling water jet first hit the hot plate. Meanwhile, the interference effect appeared gradually in the interference region, and the heat transfer coefficient curve showed a trend similar

Fig. 13 The heat transfer coefficient distribution with flow rate of $t = 15$ s ($P = 150$ mm)



to that of the flow region. In addition, it could be observed that the heat transfer coefficient in the interference region was obviously larger than that for the flow region when the interference effect occurred.

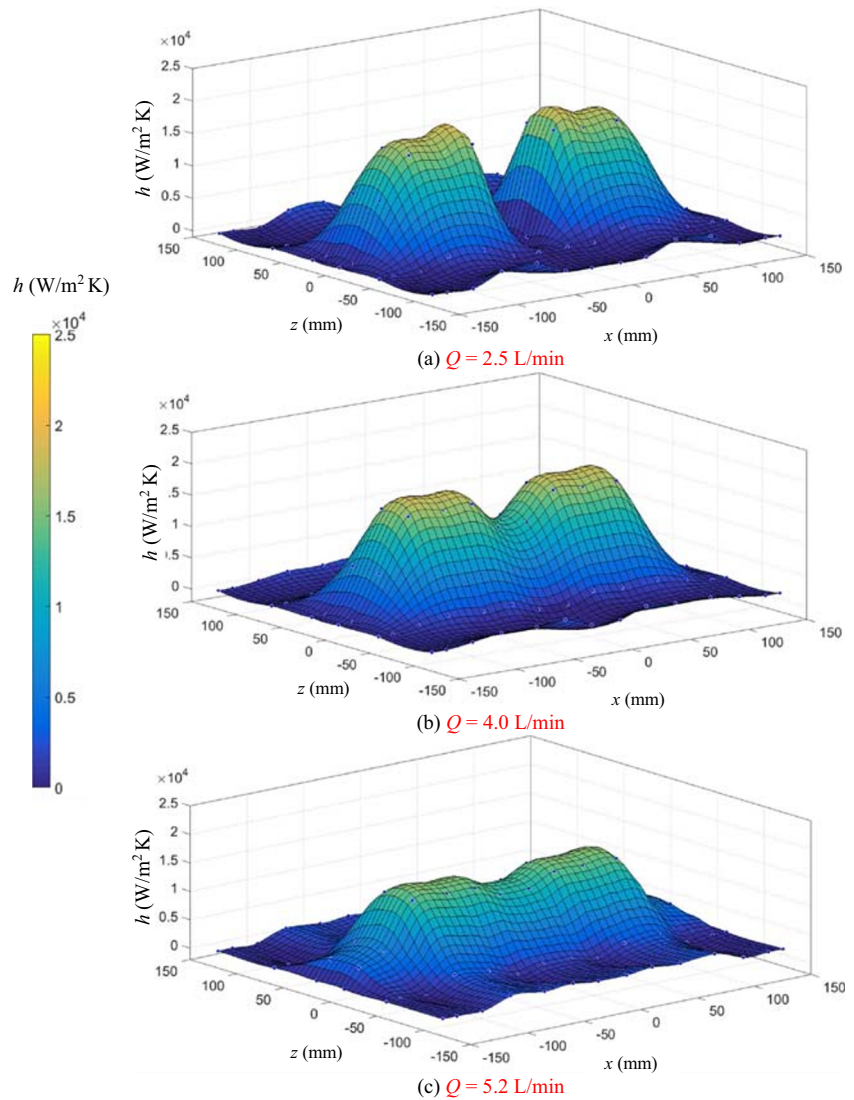
Figure 16 indicates shows the heat flux curves during the cooling process at a pitch of 150 mm and a water flow rate of 5.2 L/min for the different regions at an initial temperature of 400 °C. As shown in Fig. 15, points 8, 1, and 6 were used to analyze the characteristics of the heat flux distribution for the impingement region, flow region, and the interference region, respectively. For point 8 (in the impingement region), the peak of the heat flux curve occurred about at $t = 1$ s, and the peak in this region appeared before the other regions. In addition, the peaks of the heat flux curves can be seen due to the arrival of the wet front. The heat flux peaks are shown to decrease as they move away from the impingement region.

Figure 17 shows the effect of water flow rate on the average heat transfer coefficient for the flat plate with a pitch of 150 mm. It can be observed that the average heat transfer

coefficient of the plate increased obviously with increases in the water flow rate because the range of the impingement region and the interference effect increased with increases in the water flow rate. The appeared time of maximum average heat transfer coefficient varied with flow rate. Meanwhile, Fig. 17 shows that the differences among the average heat transfer coefficient curves decreased with increases in the cooling time. The range of the average heat transfer coefficient was about 1200 ~ 4021 W/(m²K), 2355 ~ 4820 W/(m²K), and 4016 ~ 5610 W/(m²K), corresponding with the water flow rate $Q = 2.5, 4.0,$ and 5.2 L/min, respectively.

Figure 18 shows the effect of the pitch of nozzles on the average heat transfer coefficient for the flat plate with w water flow rate of 5.2 L/min. It can be seen that the peak of the average heat transfer coefficient occurs simultaneously regardless of the nozzle pitch. However, the peak value of the average heat transfer coefficient curves increases with decreases in the pitch. That was attributed to the interference effect since a pitch of 100 mm is obviously stronger than

Fig. 14 The heat transfer coefficient distribution with flow rate of $t = 20$ s ($P = 150$ mm)



itches of 150 mm and 200 mm. The average heat transfer coefficients with pitches of 150 mm and 200 mm were very close (within 4 s), and the difference in the average heat transfer coefficients between pitches of 150 mm and 200 mm increased due to the increase in the interference effect from 4 s to 20 s. In addition, the maximum of the average heat transfer coefficient for a pitch of 100 mm under a water flow rate of 5.2 L/min was about $6900 \text{ W}/(\text{m}^2\text{K})$.

6 Conclusion

Based on the results of the experiment, a three-dimensional model of a flat plate was built to calculate the transient heat transfer coefficient by solving the inverse heat conduction problem using a conjugate gradient method (CGM) search. In this study, dual nozzles were used to study the interference effect for a flat plate during the spray impingement cooling

process. The pitch of the nozzles and the water flow rates were considered to be important factors to analyze the characteristics of the cooling curve, the heat transfer coefficient distribution, and the heat transfer rate of the hot plate. According to the experimental and numerical results, the conclusions can be summarized as follows:

1. The flow track on a flat plate surface was divided into three parts: an impingement region, an interference region, and a flow region. The impingement region appeared as an ellipse located below the nozzles. The interference region was located in the center of the impingement regions along the short-axis, and the interference effect was obviously enhanced with increases in the water flow rate. The flow region was located around the interference and impingement regions.
2. The interference pitch increased with the water flow rate, and the height increased due to enhancement in the range of the impingement region.

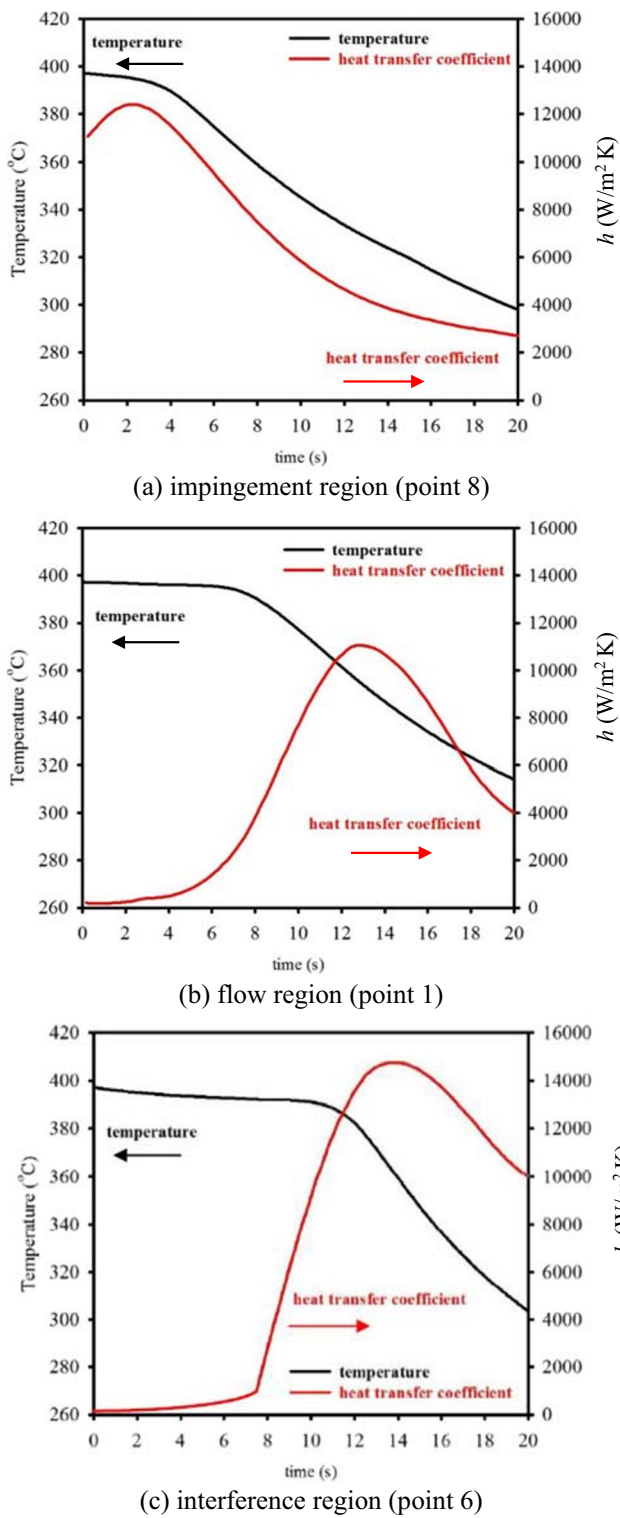


Fig. 15 Cooling curve and heat transfer coefficient distribution by region

3. When the water impinged on the hot plate, the temperature of the impingement region dropped significantly and immediately and then changed relatively slowly. At the interference and flow regions, the temperature initially changed moderately, and then a

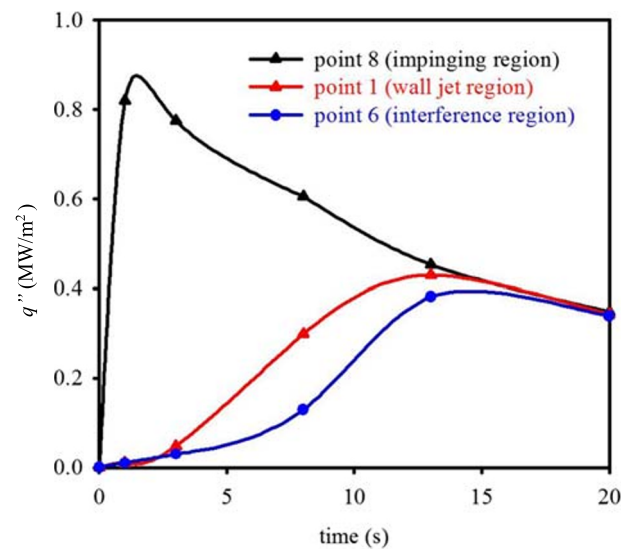


Fig. 16 Heat flux curves with different regions ($Q = 5.2$ L/min, $P = 150$ mm)

sharp drop occurred from the center to the edge sequentially.

- As the heat transfer region spread from the impingement region to the interference region, the flow region gradually grew with the water flow. The heat transfer coefficient of the impingement region was larger than other regions, and a maximum heat transfer coefficient of $23,000$ W/(m^2K) is observed. Meanwhile, the maximum heat transfer coefficient in the interference region was approximately $14,000$ W/(m^2K) during the cooling process.
- The temperature of the impingement region (point 8) decreased slowly within 4 s and then decreased rapidly. The corresponding heat transfer coefficient curve increased slightly and then decreased during the cooling process.

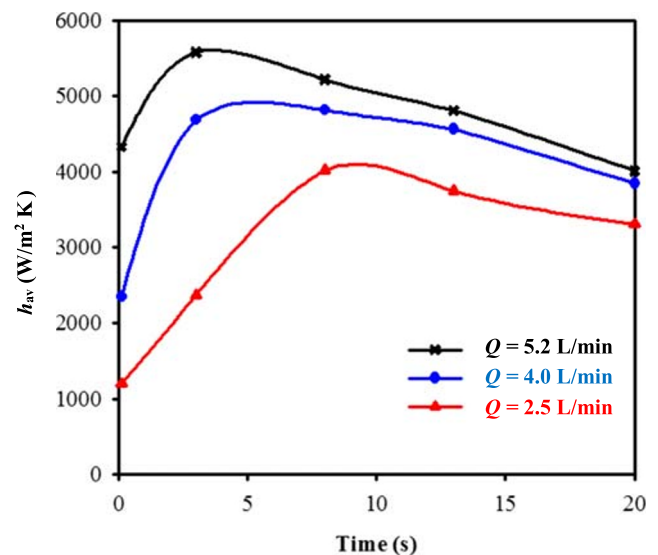


Fig. 17 The effect of water flow rate on the average heat transfer coefficient ($P = 150$ mm)

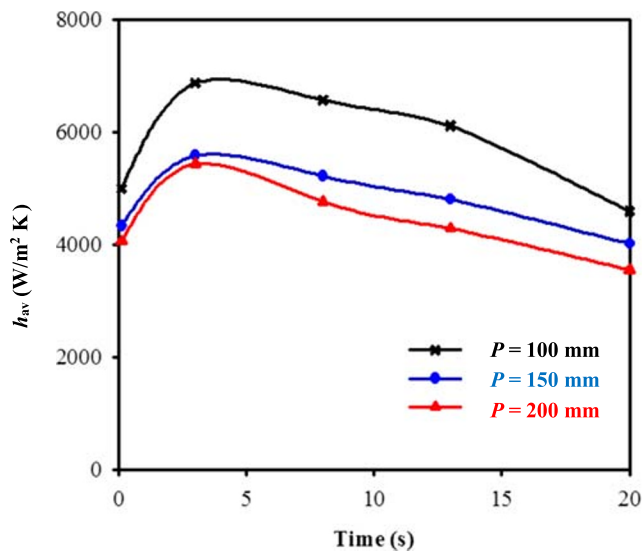


Fig. 18 The effect of different interference pitches on the average heat transfer coefficient ($Q = 5.2$ L/min).

The heat transfer coefficient of the flow region remained at a lower value until the vapor film was eliminated and then increased rapidly from 6 s to 13 s, after which it decreased. The trend of the heat transfer coefficient in the interference region was similar to that in the flow region, but was significantly larger than that in the flow region if the interference effect was generated.

- Both the water flow rate and the pitch of the nozzles affected the interference effect, where the average heat transfer coefficient increased with increases in the water flow rate but decreased with increase in the pitch.

Funding information This research was financially supported by the Ministry of Science and Technology and China Steel Corporation, Taiwan, under contract number MOST106–2221-E-006-145-MY2.

Compliance with ethical standards

Conflict of interest The authors declare that they have no conflict of interest.

References

- Chiu SL, Lin TH (2005) Experiment on the dynamics of a compound drop impinging on a hot surface. *Physics of Fluid* 17:1–9
- Leocadio H, Passos JC, da Silva AFC (2009) Heat transfer behavior of a high temperature steel plate cooled by a subcooled impinging circular water jet. 7th ECI International Conference on Boiling Heat Transfer:3–7
- Karwa N, Gambaryan-Roisman T, Stephan P, Tropea C (2011) Experimental investigation of circular free-surface jet impingement quenching: transient hydrodynamics and heat transfer. *Exp Thermal Fluid Sci* 35:1435–1443
- Gradeck M, Kouachi A, Borean JL, Gardin P, Lebouche M (2011) Heat transfer from a hot moving cylinder impinged by a planar subcooled water jet. *Int. J. Heat Mass Transf* 54:5527–5539
- Wang H, Yu W, Cai QW (2012) Experimental study of heat transfer coefficient on hot steel plate during water jet impingement cooling. *Journal of Materials Process Technology* 212:1825–1832
- Dou RF, Wen Z, Zhou G, Liu XL, Feng XH (2014) Experimental study on heat-transfer characteristics of circular water jet impinging on high-temperature stainless steel plate. *Appl Therm Eng* 62:738–746
- Fu TL, Wang ZD, Deng XT, Wang GD (2015) The influence of spray inclination angle on the ultra fast cooling of steel plate in spray cooling condition. *Appl Therm Eng* 78:500–506
- Wang BX, Lin D, Xie Q, Wang ZD, Wang GD (2016) Heat transfer characteristics during jet impingement on a high-temperature plate surface. *Appl Therm Eng* 100:902–910
- Kahani M, Jackson RG, Rosengarten G (2016) Experimental investigation of TiO₂/water nanofluid droplet impingement on nano-structured surfaces. *Ind Eng Chem Res* 55:2230–2241
- Hall DD, Mudawar I (1995) Experimental and numerical study of quenching complex-shaped metallic alloys with multiple. *Int. J. Heat Mass Transf* 7:1201–1216
- Horacek B, Kim J, Kiger KT (2004) Spray cooling using multiple nozzles: visualization and wall heat transfer measurements. *IEEE Trans Device Mater Reliab* 4:614–625
- Horsky J, Raudensky M, Tseng AA (2005) Heat transfer study of secondary cooling in continuous casting. *AISTech, Iron & Steel technology Conference and exposition*
- Shtevi T, Atal M, Rashkovan A, Katz M, Kahana E, Sher E (2008) Experimental study on the overlapping sprays cooling of hot surfaces above Leidenfrost point using industrial atomizers ILASS :1–4
- Stark P, Schuettenberg S, Fritsching U (2011) Spray quenching of specimen for ring heat treatment. *Computational Methods in Multiphase Flow* 70:201–212
- Horsky J, Kotrbacek P, Kvapil J, Schoerhuber K (2012) Optimization of working roll cooling in hot rolling. 9th International Conference on Heat Transfer, Fluid Mechanics and Thermodynamics:685–690
- Pohanka M, Votavova H (2016) Overcooling in overlap areas during hydraulic descaling. *Materials and technology* 50:575–578
- Jang JY, Hsu JF, Leu LF (2015) Optimization of the span angle and location of vortex generators in a plate-fin and tube heat exchanger. *Int. J. Heat Mass Transf* 67:432–444
- Jang JY, Tsai YG (2015) Optimization of thermoelectric generator module spacing and spreader thickness used in a waste heat recovery system. *Appl Therm Eng* 51:677–689
- Jang JY, Chen CC (2015) Optimization of louvered-fin heat exchanger with variable louver angles. *Appl Therm Eng* 91:138–150
- Jang JY, Huang JB (2015) Optimization of a slab heating pattern for minimum energy consumption in a walking-beam type reheating furnace. *Appl Therm Eng* 85:313–321
- Gan YF, Jang JY (2017) Optimal heat transfer coefficient distributions during the controlled cooling process of an H-shape steel beam advances in materials science and engineering :1–15
- Bergman TL, Lavine SL (2016) Fundamentals of heat and mass transfer, eighth edition, Wiley
- Kline SJ, McClintock FA (1953) Describing the uncertainties in experimental ASME. *Mech Eng* 75:3–8

Publisher's note Springer Nature remains neutral with regard to jurisdictional claims in published maps and institutional affiliations.